Article

Geostationary sensor based forest fire detection and monitoring: an improved version of the SFIDE algorithm

Valeria Di Biase [1], Giovanni Laneve [2]

[1] Dipartimento di Ingegneria Astronautica, Elettrica e Energetica – Sapienza Università di Roma; valeria.dibiase@uniroma1.it
[2] Scuola di Ingegneria Aerospaziale; giovanni.laneve@uniroma1.it

Abstract: The paper aims at presenting the results obtained in the development of a system allowing the detection and monitoring of forest fires and the continuous comparison of their intensity when several events occur simultaneously, as usually happens in the European Mediterranean countries during the summer season. The system, called SFIDE (Satellite FIre DEtection), exploits a geostationary satellite sensor (SEVIRI on board of MSG satellite series). The algorithm was developed several years ago in the framework of a project (SIGRI) funded by the Italian Space Agency (ASI). This algorithm has been completely reviewed in order to enhance its efficiency by reducing false alarms rate preserving a high sensitivity. Due to the very low spatial resolution of SEVIRI images (4x4 km^2 at Mediterranean latitude) the sensitivity of the algorithm should be very high to detect even small fires. The improvement of the algorithm has been obtained by: introducing the sun elevation angle in the computation of the preliminary thresholds to identify potential thermal anomalies (hot spots), introducing a contextual analysis in the detection of clouds and in the detection of night-time fires. The results of the algorithm have been validated in the Sardinia region by using ground true data provided by the regional Corpo Forestale e di Vigilanza Ambientale (CFVA). A significant reduction of the commission error (less than 10%) has been obtained with respect to the previous version of the algorithm and also with respect to fire-detection algorithms based on low earth orbit satellites.

Keywords: satellite; wildfire; detection

1. Introduction

Every year, annual reports highlight the extent of the forest fires phenomenon in the European Union, where more than half a million ha of forests burn in about 65000 fires (Figure 1) [1]. This phenomenon is particularly relevant in the European Mediterranean region, where climatic factors produce a high level of vegetation stress during the summer months which causes a higher risk of inflammability.

In Italy, the amount of wildland and forest areas that burns each year is, on average, 50,000 ha, and this phenomenon is particularly relevant in regions such as Sardinia, where, from 1995 to 2009, an area of 16600 ha per year burnt, and over 90% of these fires were human-induced [2].

For this reason, the adoption of a system capable of detecting as early as possible the trigger of new fires would considerably reduce environmental, material and social damage [3].

The use of satellite systems, developed since the early '60s of the last century by the US Forest Service [4], can be an extraordinary tool to detect hotspots and evaluate the vegetation stress level.

A first classification of fire detection algorithms using remote data, distinguishes between those in which information is provided by a single channel (*one-channel* algorithms), and those in which data are provided from two or more channels (*multi-channel* algorithms). In both cases, it is essential to have information in the MWIR (Medium Wave InfraRed) region of the spectrum, and in particular in channels around 3.9 μm: the radiative emission peak for temperatures that characterize forest fires

Preprints (www.preprints.org) | NOT PEER-REVIEWED | Posted: 2 January 2018 doi:10.20944/preprints201801.0007.v1

(800-1500 K) is in the range of 2-4 μm and, moreover, it is possible to work in atmospheric windows. In the case of multi-channel systems, it is common practice to choose a second channel in the TIR (Thermal InfraRed) region, at wavelengths between 8 μm and 12 μm, where the emission of bodies at temperatures close to those characterizing the Earth's surface is maximum.

Most of current multi-channel algorithms use band at 3.9 μm in combination with band at 10.8 μm, available for the major satellite sensors used for fire detection. Remote data in these channels are often accompanied by the VIS bands, used for the detection of pixels with cloud coverage and for the detection of false alarms.

A further distinction concerning fire detection systems is based on the characteristics of the orbit in which the satellite is located. For low orbit, the advantage of having images at a higher spatial resolution is accompanied by a low frequency of observation (approximately, two observations per day). Using instead weather satellites located in geostationary orbit, it is possible to have a continuous monitoring (images are usually acquired every 15' or 30'), but with a significantly lower spatial resolution (from 3 to 5 km per pixel, depending on latitude). Despite the disadvantages of low spatial resolution as the minimum dimensions of detectable fires, this last solution is useful for the purpose of real-time monitoring.

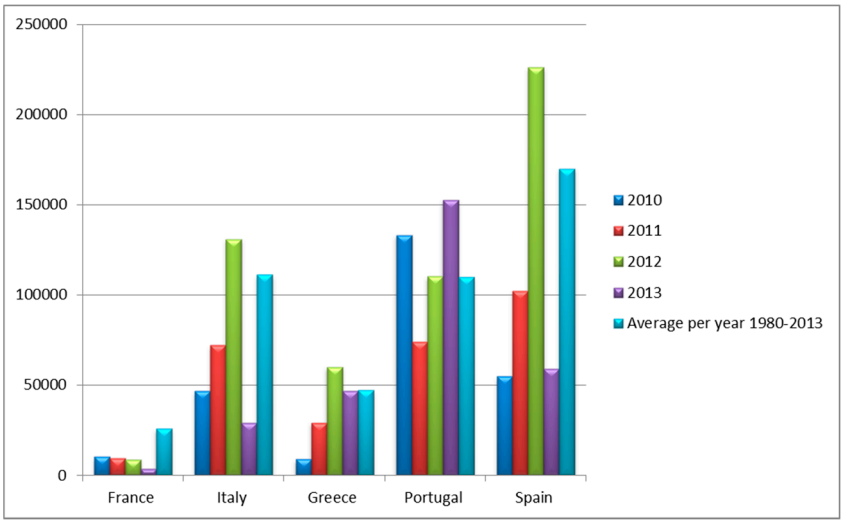

Figure1. Averaged annual burned area in the European countries most affected by fires between 1980 and 2013, compared with more recent years.

MODIS (Moderate Resolution Imaging Spectroradiometer) and AVHRR (Advanced Very High Resolution Radiometer) are among the most commonly used low orbit satellite sensors for forest fire monitoring.

MODIS radiometer allows the detection of data in 36 spectral bands from VIS to TIR with resolution of 250 m for channels 1-2, 500 m for channels 3-7, and 1 km for the remaining bands. MODIS sensors are located on NASA Aqua and Terra satellites. These two complementary satellites, allow the detection of images of the same region four times per day, recording two images during diurnal hours and two during nocturnal hours [5]. The works of Kaufman [6], Justice [7] and Giglio [8-10] are the most relevant for fire detection using MODIS data. AVHRR/3 is the third and last generation of the radiometer developed by NOAA (National Oceanic and Atmospheric Administration) in collaboration with NASA, used since 1978. It has 6 radiometric channels with 1 km resolution, and its orbit permits the acquisition of one or two images of the same area per day.

For fire detection using AVHRR data, the works of Robinson [11], Flasse and Ceccato [12] and Giglio [8,13] are of primary importance. Finally, geostationary satellites of the MSG series, operated by EUMETSAT consortium, are of great interest for the present work. The SEVIRI sensor on board of MSG satellite can acquire images every 15 minutes, in twelve channels: three in Visible and Near Infra-Red (VNIR), and eight in Infra-Red (IR). These images have 3 km resolution at the sub-satellite

 doi:10.20944/preprints201801.0007.v1

point (the equator), with the exception of the High Resolution Visible (HRV) channel (12th), which provides 1 km resolution images [14].

For fire detection using MSG-SEVIRI data, works of Calle [15], Laneve [16], Roberts e Wooster [17] and Amraoui [18] are relevant. Calle proposes an algorithm capable of detecting fire with a minimum dimension of 0.7 ha on the Iberian land; Laneve shows a process for real-time coverage in Mediterranean area; Roberts and Wooster propose an algorithm in which false detection is less than 4% of observed fires; lastly, Amraoui proposes an algorithm for live coverage and combusted area rates on Africa.

Mediterranean areas are at the highest risk and suffer great losses of infrastructures, forested and agricultural land, human and livestock lives. The risk of such fires is expected to increase in forthcoming years under the impact of climate changes; vegetation becomes more inflammable (due to thermal stress and drought) and fire services are faced with difficulties when trying to suppress a fire due to increased inflammability and water shortage [3].

Previous studies demonstrate the capabilities of SEVIRI to detect fires, despite its low spatial resolution. In the Mediterranean areas thanks to its geostationary orbit, it can drastically reduce the reaction times compared to fire-detection based on low orbit systems. The main purpose of this paper is to show the utility of geostationary systems (MSG/SEVIRI) for fire-detection, focusing on fire occurrences on the Sardinian island, characterized by a non-homogeneous coverage and high anthropization, issues neglected by current literature. In 2008, SIGRI (Sistema Integrato per la Gestione del Rischio Incendi) project was funded by ASI (Agenzia Spaziale Italiana) to face natural and human-induced disaster, and to demonstrate the abilities of supporting risk assessment, monitoring and management of fire by using remote-sensing satellite systems [19-21].

SEVIRI sensor is showing its ability to guarantee a live coverage by sending data every fifteen minutes. The CRPSM (Centro di Ricerca Progetto San Marco) has been studying for several years the possibility of using images acquired by SEVIRI: SFIDE (System for FIre DEtection) algorithm, presented in this paper, has been developed to exploit the images high update frequency by comparing temperature variation in subsequent images (change-detection), by using thresholds fit on the Sardinian island.

The paper is organized as follows: section 2.1 describes exploited data and method for real time coverage, section 2.2 describes SFIDE algorithm with its thresholds; section 3 shows achieved results with a comparison in the Sardinian area between hot spots detected by SFIDE, ground data provided by forest rangers CFVA (Corpo Forestale e di Vigilanza Ambientale) and hot spots detected by low orbit based fire-detection system.

2. Data and Methodology

The most common algorithms developed in the last decade, use remote data from low orbit satellite sensors (MODIS, AVHRR) or geostationary orbit satellite sensor (SEVIRI, GOES Imager) to apply absolute thresholds or contextual tests and obtain hot-spots as output results, together with the characterization of the fire pixels. In section 2.1 a model of fire-detection algorithm and a description of input data is shown; in section 2.2 how SFIDE algorithm uses absolute and contextual tests together with an innovative change-detection method to obtain a continuous monitoring of interested area from geostationary orbit data is illustrated.

2.1. Data & Methods

The European MSG satellite series are geostationary meteorological satellites operated by the EUMETSAT consortium. The most important sensor for the purpose of this paper is the Spinning Enhanced Visible and Infrared Imager (SEVIRI), comprising 11 spectral bands and a visible broadband (HRV). SEVIRI spatial resolution is 3 km at nadir, 1 km for HRV channel. The scan of the full disk is completed every 15 min, 5 min for the rapid scanner modality (RSS). SEVIRI has three visible bands (broadband centered at 0.75 μm, 0.63 μm and 0.81 μm), one near-infrared (1.6 μm) and 8 infrared bands (3.9, 6.2, 7.3, 8.7, 9.7, 10.8, 12.0 and 13.4 μm) [Table 1].

Preprints (www.preprints.org) | NOT PEER-REVIEWED | Posted: 2 January 2018 doi:10.20944/preprints201801.0007.v1

Main applications of SEVIRI scanner are [22]: cloud detection through VIS 0.6 and VIS 0.8 channels; aerosol, soil humidity and vegetation index retrieval (IR 1.6, VIS 0.6, VIS 0.8); water vapor and wind determination (IR 6.2, IR 7.3); clouds and their temperature (IR 3.8, IR 8.7, IR 10.8, IR 12.0); high-atmosphere monitoring (IR 9.7); pressure at high altitude (IR 13.4).

SFIDE algorithm uses IR 3.8, IR 10.8, IR 12.0, VIS 0.6, VIS 0.8 for fire detection and estimation of surface temperature.

Table 1. Bands of SEVIRI radiometer (www.esa.int).

Channel	Spectral Band	Wavelenght (μm)	Central Wavelenght (μm)	Equator Resolution (km)
1	VIS 0.6	0.56 – 0.71	0.635	3
2	VIS 0.8	0.74 – 0.88	0.81	3
3	IR 1.6	1.50 – 1.78	1.64	3
4	IR 3.9	3.48 – 4.36	3.92	3
5	WV 6.2	5.35 – 7.15	6.25	3
6	WV 7.3	6.85 – 7.85	7.35	3
7	IR 8.7	8.30 – 9.10	8.70	3
8	IR 9.7	9.38 – 9.94	9.66	3
9	IR 10.8	9.80 – 11.80	10.80	3
10	IR 12.0	11.00 – 13.00	12.00	3
11	IR 13.4	12.40 – 14.40	13.40	3
12	HRV	0.60 - 0.90	0.75	1

A model of fire-detection algorithm using remote sensing data is presented in Figure 2. The SEVIRI images are directly acquired at the University of Rome premises through the EUMETCAST service. After preliminary operations, consisting in the selection of interested area and the application of a sea-mask to exclude pixels in sea area, it is necessary to assume black body simplification ($\varepsilon=1$) for the evaluation of brightness temperature (T_b) whereas reflectance (r_{ch}) in VIS channels is retrieved knowing the values of radiance (R), Digital Number (DN), calibration coefficient (c_f) and Offset (R_0), data contained in the heading of *pgm* format SEVIRI images.

One of the most common causes of false alarm in fire detection is the presence of clouds within the pixel, as clouds have similar features to fires: increase of T_b in MIR channel at 3.9 μm ($T_{b3.9}$) due to a major reflection of sunlight, decrease of T_b in TIR channel at 10.8 μm ($T_{b10.8}$), a consequent increase of brightness temperature difference (ΔT) between 3.9 μm and 10.8 μm channel. Various methods are adopted to detect cloud pixels. An algorithm similar to the one proposed by Saunders and Kriebel for AVHRR sensor [23] will be employed in this work. The algorithm applies fixed thresholds and distinguishes daily and nightly hours.

It is now possible to detect hot spots by applying specific thresholds. Using fixed thresholds for Tb3.9 and for ΔT, it is possible to distinguish two categories of pixels: non-fire pixel or potential-fire pixels. This distinction is generally made by using a multi-channel approach with fixed thresholds. A pixel is considered a potential hot-spot if it satisfies:

$$\begin{cases} T_{b3.9} > T_{b3.9MIN} \\ \Delta T = T_{b3.9} - T_{b10.8} > \Delta T_{\min} \end{cases} \quad (1)$$

where $T_{b3.9MIN}$ and ΔT_{min} are threshold values of $T_{b3.9}$ and ΔT, specifically selected considering the area of interest and its coverage. Official reports by EUMETSAT apply as fixed thresholds for a potential fire-pixel: 310 K and 5 K for daytime hours and 290 K and 0 K for nocturnal hours. In the last few years, a dependence on solar elevation, or solar zenith angle (SZA) has been shown. This condition allows the avoidance of omission errors in the hours in which SZA is higher.

Fixed thresholds expressed as linear function of SZA are:

Preprints (www.preprints.org) | NOT PEER-REVIEWED | Posted: 2 January 2018 doi:10.20944/preprints201801.0007.v1

$$\begin{cases} T_{b3.9} > T_{b3.9\_0} - c_{3.9} \times SZA \\ \Delta T = T_{b3.9} - T_{b10.8} > \Delta T_0 - c_{\Delta T} \times SZA \end{cases} \quad (2)$$

where $T_{b3.9\_0}$ and ΔT_0 are constants chosen for $SZA=0°$; $c_{3.9}$ and $c_{\Delta T}$ are coefficients evaluated as 0.3 [K/deg] and 0.0049 [K/deg] [17].

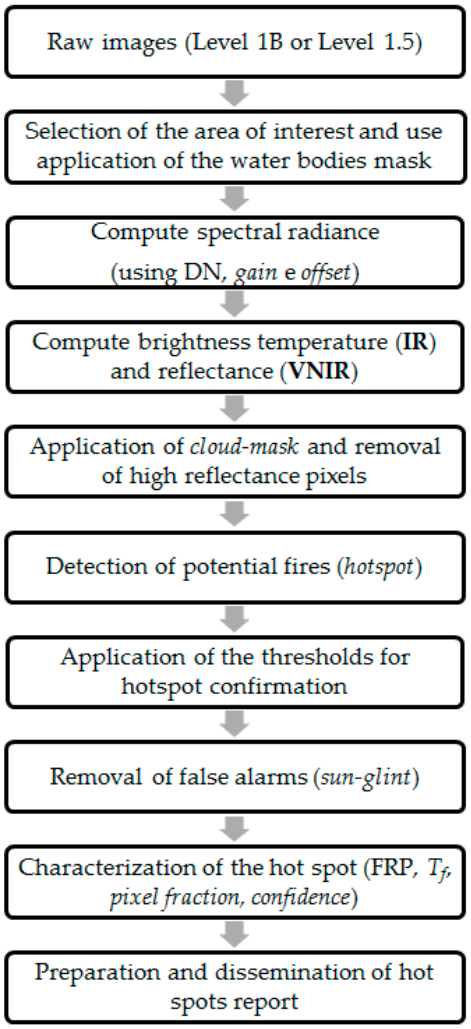

Figure 2. A model of fire-detection algorithm using remote sensing data

The algorithm usually continues by applying contextual thresholds, in some cases used for the validation of fire points [12, 17], in other cases used as test for hot-spot detection [6, 13]. Contextual algorithm is based on average values of $T_{b3.9}$, ΔT and their standard deviations ($\delta_{T_{b3.9}}$ e $\delta_{\Delta T}$) in $n \times n$ regions centered on the supposed fire point (from 3x3 to 5x5 pixels in case of GEO satellite based systems, to 21x21 pixels for LEO satellite). Thresholds for the detection of fire points are:

$$\begin{cases} T_{b3.9} > \overline{T_{b3.9}} + k_{T_{b3.9}} \cdot \delta_{T_{b3.9}} - k_0 \\ \Delta T > \overline{\Delta T} + \max(k_{\Delta T} \cdot \delta_{\Delta T}, \Delta T_{MIN}) \end{cases} \quad (3)$$

where $\overline{T_{b3.9}}$ and $\overline{\Delta T}$ are average values of $T_{b3.9}$ and ΔT in $n \times n$ region; $k_{T_{b3.9}}$ e $k_{\Delta T}$ are dimensionless coefficients with values ranging from 2 to 4; k_0 is a constant between 0 K and 3 K; ΔT_{MIN} is a constant between 2.5K and 6 K; $\max(k_{\Delta T} \cdot \delta_{\Delta T}, \Delta T_{MIN})$ is an operator that returns the

Preprints (www.preprints.org) | NOT PEER-REVIEWED | Posted: 2 January 2018 doi:10.20944/preprints201801.0007.v1

maximum value between $k_{\Delta T} \cdot \delta_{\Delta T}$ and ΔT_{MIN}. Giglio suggests for MODIS sensor: $k_{T_{b3.9}} = 3$, $k_{\Delta T} = 3.5$, $k_0 = 0$ K, $\Delta T_{MIN} = 6$ K [10]. Robert and Wooster suggest for SEVIRI sensor: $k_{T_{b3.9}} = 2$, $k_{\Delta T} = 2$, $k_0 = 0$ K, $\Delta T_{MIN} = 2.5$ K [17].

A further cause of false alarm is the sun-glint phenomenon, or the reflection of sunlight on water mirrors that causes an increase of $T_{b3.9}$ and ΔT. If there is a correspondence between the angle value (ϑ_g) between the line connecting surface-satellite and the specular direction to the solar radiation affecting the water mirror (Figure 3), then high risk for coast line pixels occurs.

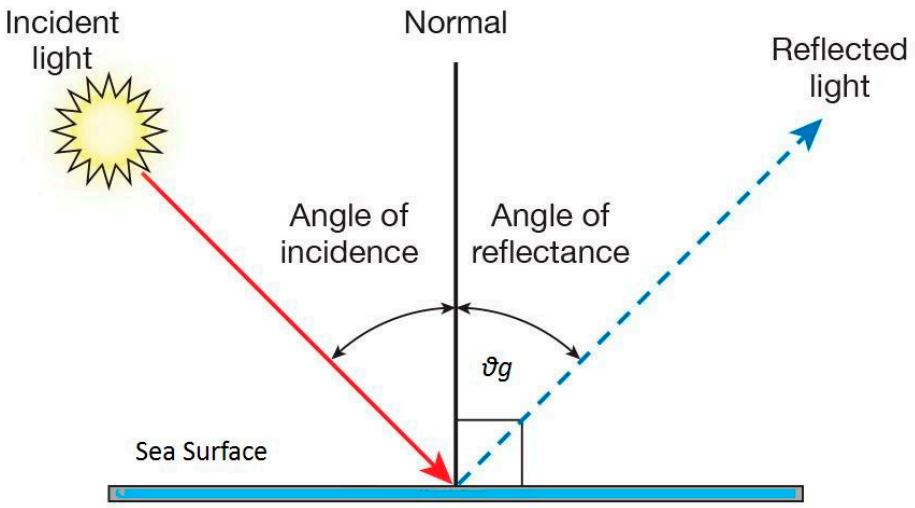

Figure 3. Sun glint, angle of reflectance (picture from the web).

Even if water bodies are excluded from the analysis by applying a mask, the phenomenon could occur at water-land border pixels. This is particularly evident in GEO systems due to their low resolution, and it is given by ground and water co-presence in the same pixel, that lead to a contamination of the contextual algorithm.

More selective thresholds or further tests are therefore used for coast line pixels. Giglio [10] suggests for MODIS satellite:

$$\begin{cases} \vartheta_g < 2^\circ \\ or \\ \vartheta_g < 10^\circ \ \text{and} \ r_{0.6} > 0.1 \ \text{and} \ r_{0.8} > 0.2 \ \text{and} \ r_{2.1} > 0.12 \\ or \\ \vartheta_g < 15^\circ \ e \ \ \mathrm{N}_w > 0 \end{cases} \quad (4)$$

where $r_{2.1}$ is the reflectance at 2.1 μm (channel 7); N_w is the amount of sea-pixels in 3x3 grid.

Hot-spots detected are now characterized in terms of dimensions (fire size in each pixel, ρ, and $A_f = \rho A_{PIXEL}$, where A_{PIXEL} is the area of a pixel [m²]), fire temperature (T_f), FRP (Fire Radiative Power) and confidence level of the fire point.

Dimension and temperature of fire can be obtained by the two-channel approach (at 3.9 μm and 10.8 μm) proposed by Dozier [24], based on the estimation of the radiant components of the pixel in absence of fire.

FRP and its integration over time, FRE (Fire Radiative Energy), are further characterizations to estimate burned biomass of the pixel. In a first, two-channel approach, after solving equations

Preprints (www.preprints.org) | NOT PEER-REVIEWED | Posted: 2 January 2018 doi:10.20944/preprints201801.0007.v1

proposed in [24], T_f and ρ are obtained and it is possible to evaluate the Fire Radiative Power using Stefan-Boltzmann law [25]:

$$FRP_{SB} = A_f \cdot \varepsilon_f \cdot \sigma \cdot \left(T_f^4 - T_b^4 \right) \quad (5)$$

where FRP_{SB} is fire radiative power estimated by Stefan-Boltzmann in [W]; ε_f is the emissivity of A_f; σ is Stefan-Boltzmann constant.

Another approach is offered by Wooster equation [26], and it does not require values of T_f and ρ:

$$FRP_W = \frac{A_{PIXEL} \cdot \sigma \cdot \varepsilon_f}{a \cdot \varepsilon_{3.9}} L_{3.9} \quad (6)$$

where FRP_W is fire radiative power estimated by Wooster in [W]; $\varepsilon_{3.9}$ is the spectral emissivity at about 3.9 μm, a is a typical constant dependent from used sensor ($a=3.06x10^{-9}$ for SEVIRI).

After estimating FRP using described methods, it is possible to evaluate FRE by integrating FRP over time:

$$FRE = \int_{t_{fire}} FRP dt \quad (7)$$

where t_{fire} is the fire duration.

Using the following equation, the estimation of burned biomass (BB) is obtained [17]:

$$BB \cong C_r \cdot FRE \quad (8)$$

where $C_r = 0.368$ [kg/MJ] is combustion ratio of biomass. Combusted biomass density (ρ_B) is [26]:

$$\rho_B \cong \frac{BB}{A_f} \quad (9)$$

Finally, it is possible to estimate a quality index of hot-spot which takes into account the amount of clouds in the area of interest and their position with respect to the hot spot. Current literature provides further heuristic methods able to estimate confidence level (C) of each hotspot, as the one proposed by Giglio for MODIS [8].

The data used to validate the results of the algorithm herein described include:

- Fire events reported by CFVA (Corpo Forestale e di Vigilanza Ambientale) of the Sardinia Region, that is the agency involved in the fire-fighting;
- Hot spots detected by the MODIS and VIIRS satellite sensors.

2.2. The SFIDE Algorithm

In this section SFIDE algorithm and its innovative aspects are described. It is important to highlight that the algorithm has been developed to be efficient in Mediterranean areas and, in particular, validation tests have been carried out in Sardinia. The complexity of the area of interest, because of its non-homogeneous and anthropized coverage, led to the elaboration of different conditions compared to the ones used in current literature.

Because of its objective to perform real time monitoring using geostationary satellite, one of the innovation of SFIDE algorithm consists in fire detection based on *change-detection* thresholds, evaluated at 15 min and 30 min intervals. Anomalous variations of $T_{b3.9}$ and ΔT in these intervals are considered as a sign of new fire event.

Preprints (www.preprints.org) | NOT PEER-REVIEWED | Posted: 2 January 2018 doi:10.20944/preprints201801.0007.v1

Further innovation is the introduction of thresholds which aim at detecting fire pixels using statistical analysis of $T_{b3.9}$ and ΔT third degree function of *SZA*: false alarms due to fixed thresholds have been overcome, as well as the ones due to linearly dependent thresholds by *SZA*.

The SFIDE algorithm prospect for diurnal data analysis (*SZA*<*85°*) is shown in Figure 4. Principal steps of the algorithm are the following:

- Preliminary operations and applications of masks;
- Fixed thresholds;
- Potential hot-spot detection;
- Hot-spot confirmation;
- Hot-spot characterization.

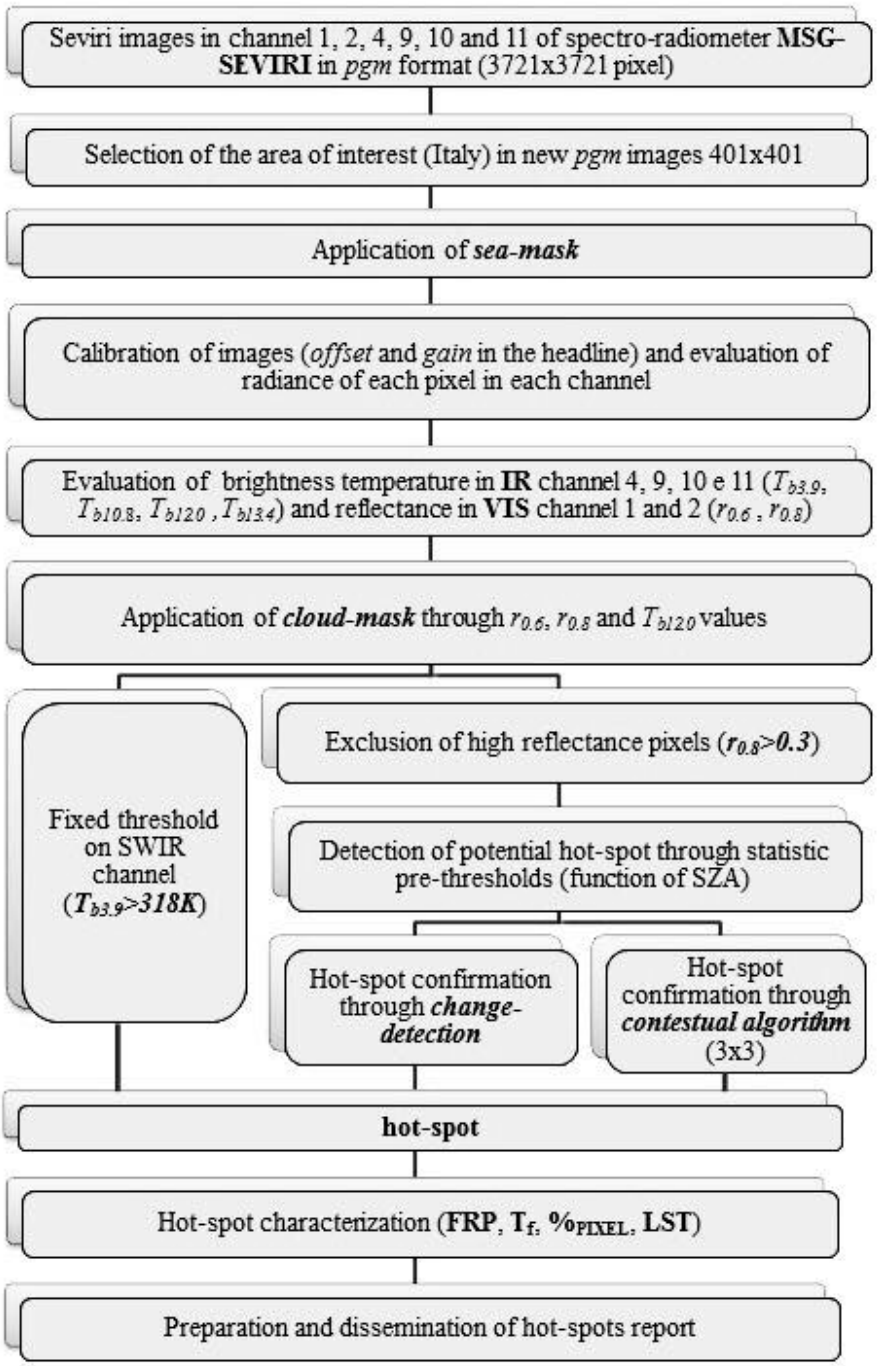

Figure 4. SFIDE algorithm prospect for diurnal data analysis.

Preprints (www.preprints.org) | NOT PEER-REVIEWED | Posted: 2 January 2018 doi:10.20944/preprints201801.0007.v1

2.2.1. Preliminary Operations

The first significant stage consists in applying typical preliminary operation: the selection of the area of interest, application of the *sea-mask* (Figure 5) and transformation of the DN (Digital Number) in radiances and then in reflectances (channels 1, 2) and brightness temperatures (channels 4, 9, 10, 11).

Figure 5. *Sea-mask*: black regions represent occulted pixels.

Next step is the application of a cloud-mask including new thresholds appropriately modified to be applied to Sardinia, as the introduction of thresholds on channel 2 and its relative reflectance ($r_{0.8}$). Similarly to [23], a pixel is considered as cloud covered if it satisfies:

$$\begin{cases} r_{0.6} + r_{0.8} > 1 \\ or \\ Tb_{12.0} < 265K \\ or \\ r_{0.6} + r_{0.8} > 0.7 \text{ 阈值 } Tb_{12.0} < 285K \end{cases} \quad (9)$$

Other pixels, even not masked as cloudy could be excluded by the algorithm because of their high reflectance.

Reflectance in channel 2 is also used to exclude partly covered pixels because of their high reflectance, which could cause false alarms, and also pixels that satisfy:

$$r_{0.8} > 0.35 \quad (10)$$

are excluded.

Value in Eq (10) is more flexible than the one proposed in [13] to reduce omission errors due to the exclusion of elevated reflectance pixels.

The importance of excluding cloudy pixels will be shown again in the step of hotspot confirmation.

Preprints (www.preprints.org) | NOT PEER-REVIEWED | Posted: 2 January 2018 doi:10.20944/preprints201801.0007.v1

2.2.2. Fixed Thresholds

Omission errors can occur when both (9) and (10) are implemented; to avoid this, a fixed threshold has been imposed on $T_{b3.9}$:

$$T_{b3.9} > 318K \tag{11}$$

Pixels that satisfy (11) are classified as hot-spots. Temperature of 318 K has been chosen after analysis of $T_{b3.9}$ trend in the considered area. As shown in Figure 4, this represents the first test used to detect hot-spots.

2.2.3. Potential Hot-Spot Detection

Two kinds of thresholds are used to detect hot-spots: fixed thresholds and SZA dependent thresholds. Thresholds expressed as linear function of SZA are generally preferred to the fixed ones, but omission and commission errors are not avoided. To model with more accuracy the average values of $T_{b3.9}$ and ΔT, an analysis of their average trend as function of SZA on Sardinia has been conducted. Their trend and their standard deviation have been stored and described by a third degree function, used as potential hot-spot detection threshold. Obtained functions are:

$$\langle T_{b3.9} \rangle = \mp 6.24\text{E-}6 \cdot \text{SZA}^3 - 0.0027 \cdot \text{SZA}^2 \pm 0.052 \cdot \text{SZA} + 305.43 \tag{12}$$

$$\langle \Delta T \rangle = \mp 4.75\text{E-}6 \cdot \text{SZA}^3 - 0.0011 \cdot \text{SZA}^2 \pm 0.018 \cdot \text{SZA} + 3.69 \tag{13}$$

where $\langle T_{b3.9} \rangle$ and $\langle \Delta T \rangle$ are respectively expected values of $T_{b3.9}$ and ΔT as a function of SZA. In the terms with odd exponent, the use of superior sign is for post-meridian hours, and inferior sign is for anti-meridian hours. A pixel is considered a hot-spot if it satisfies:

$$\begin{cases} T_{b3.9} > \langle T_{b3.9} \rangle \\ \Delta T = T_{b3.9} - T_{b10.8} > \langle \Delta T \rangle \end{cases} \tag{14}$$

2.2.4. Hot-Spot Confirmation

At this stage, checks on potential hot-spots are carried out to confirm them. Checks follow two paths: change-detection and contextual analysis. For both methodologies, narrower thresholds have been used for high false alarm risk pixel due to its partial cloud coverage, sudden change in reflection over time, or Sun-glint.

Change-detection: This innovative approach is particularly efficient in detecting new fires earlier than contextual analysis. Statistical analysis has been conducted on average trend of $T_{b3.9}$ and ΔT as function by SZA at 15 and 30 minutes intervals. Data on their average variations have been interpolated in third degree function dependent on SZA and used as *pre-thresholds*. Lastly, these functions have been used to evaluate a kind of thresholds, named *trigger thresholds*, that allow one to confirm fires in growing phase because of the joint increase of $T_{b3.9}$ and ΔT above statistically evaluate values.

The following symbolism has been used:

- $T_{b3.9\_15'}$ and $\Delta T_{15'}$: $T_{b3.9}$ and ΔT values for image that precedes by 15 minutes the current one;
- $T_{b3.9\_30'}$ and $\Delta T_{30'}$: $T_{b3.9}$ and ΔT values for image that precedes by 30 minutes the current one;
- $\Delta T_{b3.9\_15'} = (T_{b3.9} - T_{b3.9\_15'})$ and $\Delta(\Delta T)_{15} = (\Delta T - \Delta T_{15'})$: $T_{b3.9}$ and ΔT variations between current image and the one that precedes at 15 minutes;
- $\Delta T_{b3.9\_30'} = (T_{b3.9} - T_{b3.9\_30'})$ and $\Delta(\Delta T)_{30} = (\Delta T - \Delta T_{30'})$: $T_{b3.9}$ and ΔT variations between current image and the one that precedes at 30 minutes.

Preprints (www.preprints.org) | NOT PEER-REVIEWED | Posted: 2 January 2018 doi:10.20944/preprints201801.0007.v1

For the thermal variations of 15 minutes, evaluated as $\Delta T_{b3.9\_15'}$ and $\Delta(\Delta T)_{15'}$ trend and their respective standard deviations are:

$$\left\langle \Delta T_{b3.9\_15'} \right\rangle = \mp 2.91\text{E-}7 \cdot SZA^3 - 1.75\text{E-}5 \cdot SZA^2 \pm 4.39\text{E-}4 \cdot SZA + 0.49 \quad (15)$$

$$\left\langle \sigma_{\Delta T_{b3.9\_15'}} \right\rangle = \pm 1.00\text{E-}6 \cdot SZA^3 - 5.09\text{E-}5 \cdot SZA^2 \mp 1.77\text{E-}2 \cdot SZA + 0.21 \quad (16)$$

$$\left\langle \Delta(\Delta T)_{15'} \right\rangle = \pm 5.03\text{E-}7 \cdot SZA^3 - 1.21\text{E-}6 \cdot SZA^2 \mp 6.84\text{E-}3 \cdot SZA + 0.005 \quad (17)$$

$$\left\langle \sigma_{\Delta(\Delta T)_{15'}} \right\rangle = \mp 7.17\text{E-}7 \cdot SZA^3 - 8.81\text{E-}5 \cdot SZA^2 \pm 1.75\text{E-}3 \cdot SZA + 0.85 \quad (18)$$

where $\left\langle \Delta T_{b3.9\_15'} \right\rangle$ and $\left\langle \Delta(\Delta T)_{15'} \right\rangle$ are functions that approximate the average trend of $\Delta T_{b3.9\_15'}$ and $\Delta(\Delta T)_{15'}$, while $\left\langle \sigma_{\Delta T_{b3.9\_15'}} \right\rangle$ and $\left\langle \sigma_{\Delta(\Delta T)_{15'}} \right\rangle$ are functions that approximate their respective average standard deviations. Similarly, an analysis considering 30 minute intervals has been conducted:

$$\left\langle \Delta T_{b3.9\_30'} \right\rangle = \pm 1.95\text{E-}6 \cdot SZA^3 - 1.25\text{E-}4 \cdot SZA^2 \mp 3.46\text{E-}2 \cdot SZA + 0.48 \quad (19)$$

$$\left\langle \sigma_{\Delta T_{b3.9\_30'}} \right\rangle = \mp 4.39\text{E-}7 \cdot SZA^3 - 6.07\text{E-}6 \cdot SZA^2 \pm 1.21\text{E-}3 \cdot SZA + 0.75 \quad (20)$$

$$\left\langle \Delta(\Delta T)_{30'} \right\rangle = \pm 9.13\text{E-}7 \cdot SZA^3 - 6.40\text{E-}6 \cdot SZA^2 \mp 1.34\text{E-}2 \cdot SZA + 0.026 \quad (21)$$

$$\left\langle \sigma_{\Delta(\Delta T)_{30'}} \right\rangle = \mp 1.18\text{E-}6 \cdot SZA^3 - 1.09\text{E-}4 \cdot SZA^2 \pm 3.56\text{E-}3 \cdot SZA + 1.16 \quad (22)$$

where $\left\langle \Delta T_{b3.9\_30'} \right\rangle$ and $\left\langle \Delta(\Delta T)_{30'} \right\rangle$ are functions that approximate the average trend of $\Delta T_{b3.9\_30'}$ and $\Delta(\Delta T)_{30'}$, while $\left\langle \sigma_{\Delta T_{b3.9\_30'}} \right\rangle$ and $\left\langle \sigma_{\Delta(\Delta T)_{30'}} \right\rangle$ are functions that approximate their respective average standard deviations.

Functions described in Eqq. (15)-(22) are trigger thresholds imposed on potential hot-spots that satisfy Eq. (14) to confirm fire in the pixel. Considering thermal variations in 15′, a potential hot-spot is confirmed if:

$$\begin{cases} \Delta T_{b3.9\_15'} = (T_{b3.9} - T_{b3.9\_15'}) > \left\langle \Delta T_{b3.9\_15'} \right\rangle + \left\langle \sigma_{\Delta T_{b3.9\_15'}} \right\rangle \\ \Delta(\Delta T)_{15'} = (\Delta T - \Delta T_{15'}) > \left\langle \Delta(\Delta T)_{15'} \right\rangle + \left\langle \sigma_{\Delta(\Delta T)_{15'}} \right\rangle + f_{15'}(\Delta r_{0.6}) \\ T_{b3.9} > \overline{T_{b3.9}} + 1.5 \\ \Delta T > \overline{\Delta T} + 0.5 \\ N_w + N_c = 0 \end{cases} \quad (23)$$

where $\overline{T_{b3.9}}$ and $\overline{\Delta T}$ are average values of $T_{b3.9}$ and ΔT in 3x3 grid centered on potential hot-spots; N_w and N_c are respectively number of water-pixels and cloudy-pixels in 3x3 grid centered on potential

Preprints (www.preprints.org) | NOT PEER-REVIEWED | Posted: 2 January 2018 doi:10.20944/preprints201801.0007.v1

hot-spots; $f_{15'}(\Delta r_{0.6}) = 100(r_{0.6} - r_{0.6\_15'})$ if $r_{0.6} > r_{0.6\_15'}$, with $r_{0.6\_15'}$ reflectance in channel 1 evaluated 15 minutes before current image. Function $f_{15'}$ is necessary to correct ΔT increase due to $r_{0.6}$ increase in 15′ intervals.

Considering thermal variations in 30′, a potential hot-spot is confirmed if it satisfies:

$$\begin{cases} \Delta T_{b3.9\_30'} = (T_{b3.9} - T_{b3.9\_30'}) > \left\langle \Delta T_{b3.9\_30'} \right\rangle + \left\langle \sigma_{\Delta T_{b3.9\_30'}} \right\rangle \\ \Delta(\Delta T)_{30'} = (\Delta T - \Delta T_{30'}) > \left\langle \Delta(\Delta T)_{30'} \right\rangle + \left\langle \sigma_{\Delta(\Delta T)_{30'}} \right\rangle + f_{30'}(\Delta r_{0.6}) \\ T_{b3.9} > \overline{T_{b3.9}} + 1.5 \\ \Delta T > \overline{\Delta T} + 0.5 \\ N_w + N_c = 0 \end{cases} \quad (24)$$

where $f_{30'}(\Delta r_{0.6}) = 100(r_{0.6} - r_{0.6\_30'})$ if $r_{0.6} > r_{0.6\_30'}$, with $r_{0.6\_30'}$ reflectance in channel 1 evaluated 30 minutes before current image.

Similar thresholds are applied to elevated risk of false alarm pixels:

$$\left| r_{0.6} - r_{0.6\_15'} \right| \geq 0.03 \quad (25)$$

$$\left| r_{0.6} - r_{0.6\_30'} \right| \geq 0.03 \quad (26)$$

$$\left(N_w + N_c \right) > 0 \quad (27)$$

$$\left(r_{0.8} - r_{0.6} \right) \geq 0.1 \quad (28)$$

Eq. (25), (26) are imposed to detect pixels with sudden variation of $r_{0.6}$, and consequently ΔT increase, due to cloudy sky. Eq. (27) allows the prevention of drawbacks due to coastal line ($N_w>0$) or near cloudy pixels ($N_c>0$)points.

If one of the conditions (25) – (28) is satisfied then conditions of Eq. (23) are replaced with:

$$\begin{cases} \Delta T_{b3.9\_15'} = (T_{b3.9} - T_{b3.9\_15'}) > \left\langle \Delta T_{b3.9\_15'} \right\rangle + 2 \cdot \left\langle \sigma_{\Delta T_{b3.9\_15'}} \right\rangle \\ \Delta(\Delta T)_{15'} = (\Delta T - \Delta T_{15'}) > \left\langle \Delta(\Delta T)_{15'} \right\rangle + 2 \cdot \left\langle \sigma_{\Delta(\Delta T)_{15'}} \right\rangle + f_{15'}(\Delta r_{0.6}) \\ T_{b3.9} > \overline{T_{b3.9}} + 1.5 \\ \Delta T > \overline{\Delta T} + 0.5 \\ N_w + N_c = 0 \end{cases} \quad (29)$$

while limits of Eq. (24) are replaced with:

Preprints (www.preprints.org) | NOT PEER-REVIEWED | Posted: 2 January 2018 doi:10.20944/preprints201801.0007.v1

$$\begin{cases} \Delta T_{b3.9\_30'} = (T_{b3.9} - T_{b3.9\_30'}) > \left\langle \Delta T_{b3.9\_30'} \right\rangle + 2 \cdot \left\langle \sigma_{\Delta T_{b3.9\_30'}} \right\rangle \\ \Delta(\Delta T)_{30'} = (\Delta T - \Delta T_{30'}) > \left\langle \Delta(\Delta T)_{30'} \right\rangle + 2 \cdot \left\langle \sigma_{\Delta(\Delta T)_{30'}} \right\rangle + f_{30'}(\Delta r_{0.6}) \\ T_{b3.9} > \overline{T_{b3.9}} + 1.5 \\ \Delta T > \overline{\Delta T} + 0.5 \\ N_w + N_c = 0 \end{cases} \quad (30)$$

2.2.5. Contextual Analysis

An alternative method for hot-spot confirmation is a contextual analysis that makes use of information extracted from the surrounding pixels.
Two confirmation conditions are imposed: low-probability and high-probability of fire point conditions. For low-probability condition point, the hot-spot is confirmed if:

$$\begin{cases} T_{b3.9} > \overline{T_{b3.9}} + \max(1, \sigma_{T_{b3.9}} - 3) \\ \Delta T > \overline{\Delta T} + \max(1.25, \sigma_{\Delta T}) \text{ 或 } \Delta T > \overline{\Delta T} + \min(2, \sigma_{\Delta T}) \text{ 和 } \Delta T > 4.5 \end{cases} \quad (31)$$

where $\sigma_{T_{b3.9}}$ and $\sigma_{\Delta T}$ are standard deviations of $T_{b3.9}$ and ΔT in the immediate neighborhood. If at least one condition between (25), (26), (28) or the following ones is satisfied:

$$r_{0.6} > 0.15 \quad (32)$$

$$r_{0.6} > \overline{r_{0.6}} + \sigma_{r_{0.6}} \quad (33)$$

$$\overline{r_{0.6}} < 0.1 \quad (34)$$

$$\min(r_{0.6})_{3x3} < 0.08 \quad (35)$$

the pixel is considered a high-probability fire. $\overline{r_{0.6}}$, $\sigma_{r_{0.6}}$ and $\min(r_{0.6})_{3x3}$ are respectively: average value, standard deviation and minimum value of $r_{0.6}$ in 3x3 grid.

For high-probability points, a hot-spot is confirmed if:

$$\begin{cases} T_{b3.9} > \overline{T_{b3.9}} + \max(2.5, \sigma_{T_{b3.9}} - 3) \\ \Delta T > \overline{\Delta T} + \min(4, 2 \cdot \sigma_{\Delta T}) \end{cases} \quad (36)$$

2.2.6. Hot-Spot Characterization: FRP and LST

For FRP evaluation, Wooster approximation (6) has been used [26]. FRP_W allows one to obtain T_f and ρ values. FRP values are useful to evaluate fire dimension and power, and therefore to quantify resources needed for each fire. Furthermore, imposing a limit value for FRP:

$$FRP > 40 \text{ 兆瓦 [MW]} \quad (37)$$

false alarms can be avoided.

Preprints (www.preprints.org) | NOT PEER-REVIEWED | Posted: 2 January 2018 doi:10.20944/preprints201801.0007.v1

Land Surface Temperature (LST) has been introduced in fire characterization. In future developments, LST value could be used instead of T_b for fire-detection thresholds and FRP evaluations. For LST evaluation, double split window technique (DSWT) has been used, with $T_{b10.8}$ and T_{b12} as input data [28]. Used algorithm is VZA (View Zenith Angle) dependent.

2.2.7. Nightly Hours Algorithm

For $SZA<85°$, an alternative algorithm has been used due to the absence of reflected solar component. Principal differences with the daily one are:

- Cloud-mask identified using a threshold on channel 10;
- Hot-spot detection with fixed thresholds occurs with limit values of $T_{b3.9}$ and ΔT, adapted to nocturnal hours;
- Fixed values of $T_{b3.9}$ and ΔT as hot-spot detection thresholds;
- Contextual analysis carried out by using average value of $T_{b3.9}$ and ΔT on the whole of Sardinia;
- No distinction between high and low probability fire pixels.

A model of the night-time algorithm is given in Figure 6.

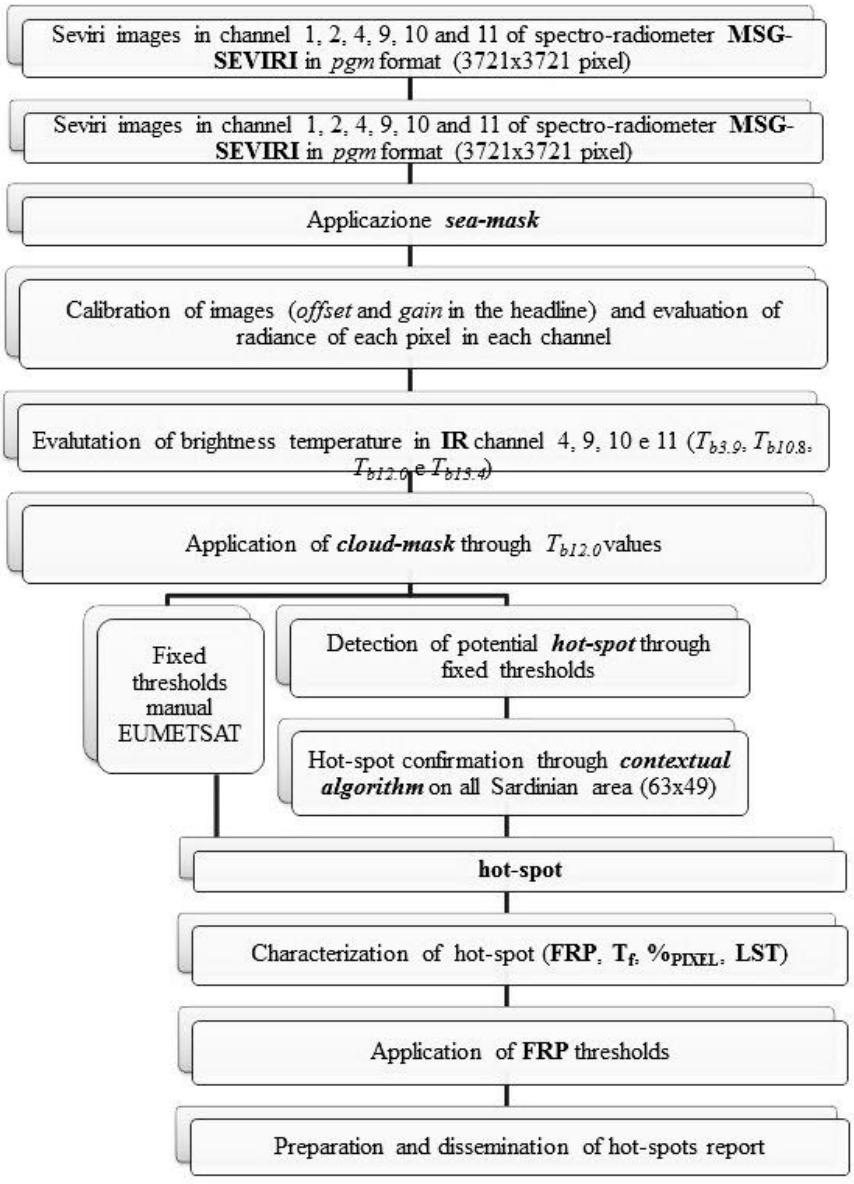

Figure 6. SFIDE algorithm prospect for nocturnal data analysis.

Preprints (www.preprints.org) | NOT PEER-REVIEWED | Posted: 2 January 2018 doi:10.20944/preprints201801.0007.v1

A pixel is considered cloudy if:

$$T_{b12.0} < 265K \tag{38}$$

Fixed thresholds based on $T_{b3.9}$ and ΔT values [29] are:

$$\begin{cases} T_{b3.9} > 290\,K \\ \Delta T > 1K \end{cases} \tag{39}$$

Due to the high number of omission errors detected using fixed thresholds, also for nocturnal hours a detection method based on fixed pre-thresholds and confirmation has been used.

A pixel is considered as potential hot-spot if it satisfies the following revised thresholds:

$$\begin{cases} T_{b3.9} > 285\,K \\ \Delta T > -2K \end{cases} \tag{40}$$

Hot-spot confirmation is made with contextual-analysis. A pixel is confirmed as hot-spot if it satisfies:

$$\begin{cases} T_{b3.9} > T_{b3.9\_SAR} + 1.5 \cdot \sigma_{T_{b3.9\_SAR}} \\ \Delta T > \Delta T_{\_SAR} + 1.5 \cdot \sigma_{\Delta T_{\_SAR}} \end{cases} \tag{41}$$

where $T_{b3.9\_SAR}$ and $\sigma_{T_{b3.9\_SAR}}$ are average values and standard deviation of $T_{b3.9}$ for the whole of Sardinia; $\Delta T_{\_SAR}$ and $\sigma_{\Delta T_{\_SAR}}$ are average values of ΔT for the whole of Sardinia.

A final confirmation is given by FRP analysis. A pixel is confirmed as hot-spot only if (37) is satisfied.

3. Data Validation

Validation of SFIDE output has been made on Sardinian area using images acquired in 2014 from 2 to 8 July and from 31 July to 6 August. These results have been compared with in situ data collected by CFVA (http://www.sardegnaambiente.it/corpoforestale/) and this comparison concerns fires detectable from geostationary orbit because of their dimension and coverage features. Another validation has been made by using the low orbit data of MODIS sensor (https://modis.gsfc.nasa.gov). It should be underlined that the fire season in the area of interest commonly goes from the 1st June to the 30th September.

3.1. Comparison with in Situ Measurements

Since CFVA measurements consist in total burned area evaluated at the end of the incendiary event, only fires larger- in total- than 5 ha have been considered. Instantaneous in situ measurements are not available, and minimum detectable fire size from geostationary orbit has been evaluated using [24] in 0.1-0.2 ha. Fires in cloudiness and high reflectance area have been excluded from the comparison. The results show that 20 of 22 detectable fires were detected (90.9 %), and only 2 fires with undefined coverage were lost, less than 10% omission errors.

Furthermore, a significant result is that not only fires that developed in forest area were detected: a certain percentage of detected hot-spots corresponds to fires that occurred in mixed or grassy covered areas.

SFIDE output consists in 285 hot-spots, of which only 14 - less than 5%- are commission errors (false alarms). Trigger thresholds (eq. 23 - 24 or 29 - 30) have been able to detect 83.53% of diurnal

Preprints (www.preprints.org) | NOT PEER-REVIEWED | Posted: 2 January 2018 doi:10.20944/preprints201801.0007.v1

detectable fires. The utility of the *change detection* based approach is confirmed by the fact that the tests of eq. 23-24 (or eq. 29-30) allow an early detection of the fires in 100% of the cases. A lower number of hot-spots has also been detected from contextual thresholds (about 50%) and fixed thresholds (about 14%).

One of the principal causes of false alarms is the sudden variation of reflectance values in channel 2, together with a sudden variation of $T_{b3.9}$ and consequently ΔT. In nocturnal hours, when these phenomena do not appear, 100% of detected hot-spots has indeed been classified as real fires. An in-depth analysis of the 14 hot-spots classified as false alarms, shows their dependence by trigger thresholds (13 out of 14 hot-spots), but the results show the importance of introducing these kinds of thresholds, not only for detecting fires non-detectable with other kinds of thresholds, but also for the purpose of using SFIDE for a real time monitoring of fire events.

An analysis of FRP values allowed the introduction of a further threshold (Eq. 44). A major restriction of this threshold value would reduce commission errors, but there would be an increase in omission ones.

Figure 7, processed with commercial software *ArcMap*, shows a comparison between SFIDE detected hot-spots (red square) and in situ measurements of CFVA (blue area) on 2, 3 and 8 of July and 5 of August 2014. Figure corresponding to 3rd July (Fig. 7b) shows non-detected fires due to a local high cloudiness. Red squares near in situ reported fires represent a kind of detected hot-spot due to sensor saturation issues.

(**a**)

(**b**)

Preprints (www.preprints.org) | NOT PEER-REVIEWED | Posted: 2 January 2018 doi:10.20944/preprints201801.0007.v1

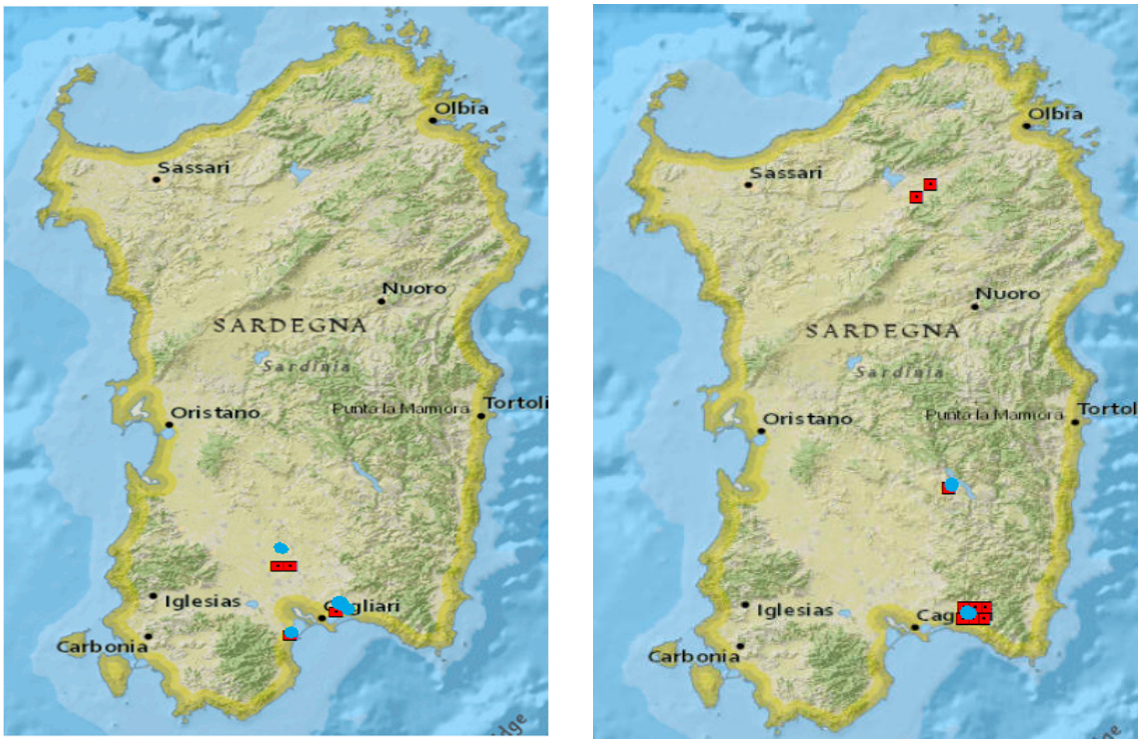

(**c**) (**d**)

Figure 7. Comparison between SFIDE detected hot-spot and CFVA measurements on 2014: 2 July **(a)**, 3 July **(b)**, 8 July **(c)** and 5 August **(d)**.

3.2. Comparison with MODIS Sensor

MODIS algorithm results over evaluated period, consist in 3 fires compared to 20 fires detected by SFIDE algorithm and 22 reported by CFVA. Only one fire was detected by MODIS sensor and non-detected by SFIDE due to a meteorological condition (local high cloudiness). These results show the importance of a geostationary orbit sensor that allows real time monitoring due to a high update frequency: 96 daily images by SEVIRI and 2-4 by MODIS. Particularly relevant is that fires larger than 100 [ha] have not been detected by MODIS sensor, and this result confirms the major advantages of SFIDE algorithm also regarding the number of detected fires.

3.3. Fire monitoring examples

Using the high refresh frequency of the SEVIRI images, in particular in the case of MSG 9 also known as RSS (Rapid Scanning Service) characterized by a refresh frequency of 5 min, it is, in general, possible to follow in a quasi-continuous way the evolution of the fire. This allows, possibly, the deduction of interesting information on the fire behavior and the effectiveness of the fire-fighting activity. Fig. 8 allows one to explain this point better. The figure compares, through the FRP (measured in MW), the behavior of two fires that occurred in the Calabria region on 20th August 2017. The behavior of one of the two fires (the one for which the FRP is shown on the left plot) seems much more 'natural' or regular than the other. Further, this fire lasts also much less than the other, about 1.5 hours (90 minutes) instead of 11 hours (660 minutes). It is also less intense reaching a maximum FRP of 180 MW instead of 330 MW, as in the case of the other fire. This suggests that fire corresponding to left plot of Fig. 8 extinguished itself for natural reasons not for the intervention of firefighters.

Preprints (www.preprints.org) | NOT PEER-REVIEWED | Posted: 2 January 2018 doi:10.20944/preprints201801.0007.v1

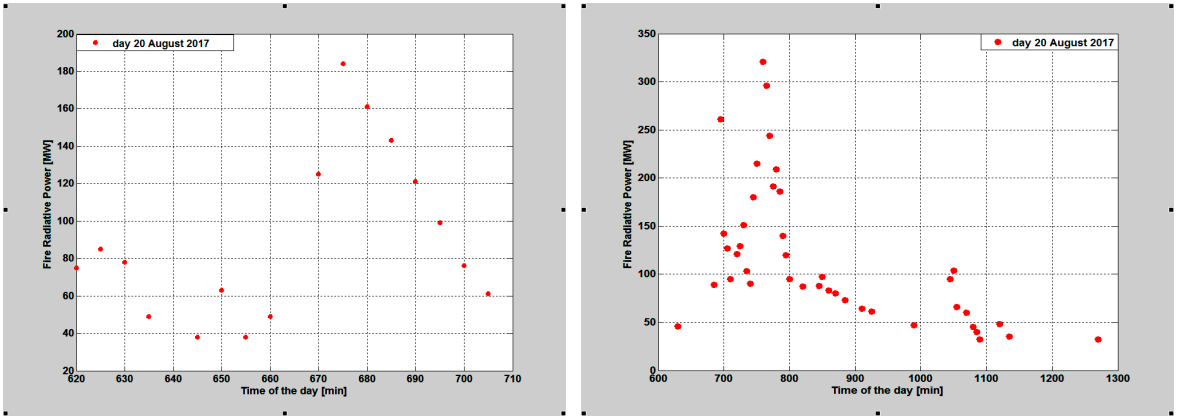

Figure 8. Comparison of the behavior of two fires that occurred on 20th August 2017 through the temporal variation of the of FRP. The fire behavior in the two cases is very different. The evolution of the fire shown in the left plot seems much more 'regular' than the one shown in the right plot.

4. Conclusions

The SFIDE algorithm was developed by authors several years ago [16] in the framework of a project funded by the Italian Space Agency devoted to implement a forest fires early detection and monitoring system based on satellite images coming from the geostationary sensor SEVIRI on board of the MSG satellites series. This paper presents a new version of the algorithm aiming, in particular, at reducing the false alarm rate. This updated version of the algorithm takes into account other previously developed methods for fire detection in order to:

- Improve the estimate of the reference temperature used to define a pixel as interested by a fire;
- Improve the cloud mask accuracy thus reducing the risk of false alarms;
- Exploit better the high refresh rate of the images to implement several tests for accurate detection of forest fires.

The results of the comparison of the events detected in Sardinia by the algorithm with those provided by local authorities and/or detected by other higher resolution satellite sensor (MODIS) confirm the improvement made. In fact, in the present version the algorithm provides an omission error of less than 10% and a commission error of less than 5%. At this point a further step is needed, which is, to reduce the approximation in the localization of the fire (the fire can occupy any position in the pixel of 4x4 km^2). At present, the position of the fire corresponds to the coordinates of the center of the pixel. Possibly exploiting the simultaneous observation from 2 geostationary satellites like MSG 8 (RSS) and MSG 9 (IODC) and introducing a fuel map of the area of interest a more accurate localization of the fire position could be achieved. This will possibly be discussed in a future paper.

References

1. Schmuck, G.; San-Miguel-Ayanz, J.; Camia, A.; Durrant, T.; Santos De Oliveira, S.; Boca, R.; Whitmore, C.; Giovando, C.; Libertà, G.; Corti, P.; Schulte, E. Forest Fires in Europe. *Publications Office of the European Union*; EUR 24910 EN, 2010.
2. Ager, A.A.; Preisler, H.K.; Arca, B.; Spano, D.; Salis, M. Wildfire risk estimation in the Mediterranean area. *Environmetrics*. **2009**, *25(6)*, 384-396.
3. Sifakis, N.I.; Iossifidis, C.; Kontoes, C.; Keramitsoglou, I. Wildfire Detection and Tracking over Greece Using MSG-SEVIRI Satellite Data. *Remote sensing*. **2011**, *3(3)*, 524-538.
4. Martín, M.P.; Ceccato, P.; Flasse, S.; Downey, I. Fire detection and fire growth monitoring using satellite data. *Remote sensing of large wildfires*; Springer: Berlin Heidelberg, Germany, 1999; pp. 101-122.

5. Salomonson, V.V.; Barnes, W.L.; Maymon, P.W.; Montgomery, H.E.; Ostrow, H. MODIS: advanced facility instrument for studies of the earth as a system. *IEEE Transactions on Geoscience and Remote Sensing*. **1989**, *27*, 145 – 153.
6. Kaufman, Y.J.; Justice, C.O.; Flynn, L.P.; Kendall, J.D.; Prins, E.M.; Giglio, L.; Ward, D.E.; Menzel, W.P.; Setzer, A.W. Potential global fire monitoring from EOS-MODIS. *Journal of Geophysical Research-Atmospheres*. **1998**, *103(D24)*, 32215-32238.
7. Justice, C.O.; Giglio, L.; Korontzi, S.; Owens, J.; Morisette, J.T.; Roy, D.; Descloitres, J.; Alleaume, S.; Petitcolin, F.; Kaufman, Y. The MODIS fire products. *Remote Sensing of Environment*. **2002**, *83(2)*, 244-262.
8. Giglio, L.; Descloitres, J.; Justice, C.O.; Kaufman, Y.J. An enhanced contextual fire detection algorithm for MODIS. *Remote Sensing of Environment*. **2003**, *87(3)*, 273-282.
9. Giglio, L.; Csiszar, I.; Restas, A.; Morisette, J.T.; Schroeder, W.; Morton, D.; Justice, C.O. Active fire detection and characterization with the advanced spaceborne thermal emission and reflection radiometer (ASTER). *Remote Sensing of Environment*. **2008**, *112(6)*, 3055-3063.
10. Giglio, L.; Schroeder, W.; Justice, C.O. The collection 6 MODIS active fire detection algorithm and fire products. *Remote Sensing of Environment*. **2016**, *178*, 31-41.
11. Robinson, J.M. Fire from space: Global fire evaluation using infrared remote sensing. *International Journal of Remote Sensing*. **1991**, *12(1)*, 3-24.
12. Flasse, S.P.; Ceccato, P. A contextual algorithm for AVHRR fire detection. *International Journal of Remote Sensing*. **1996**, *17(2)*, 419-424.
13. Giglio, L.; Kendall, J.D.; Justice, C.O. Evaluation of global fire detection algorithms using simulated AVHRR infrared data. *International Journal of Remote Sensing*. **1999**, *20(10)*, 1947-1985.
14. Aminou, D.M.A. MSG's SEVIRI instrument. *ESA Bulletin (0376-4265)*. **2002**, 111, 15-17.
15. Calle, A.; Casanova, J.L.; Romo, A. Fire detection and monitoring using MSG Spinning Enhanced Visible and Infrared Imager (SEVIRI) data. *Journal of Geophysical Research: Biogeosciences*. **2006**, *111(G4)*.
16. Laneve, G.; Castronuovo, M.M.; Cadau, E.G. Continuous monitoring of forest fires in the Mediterranean area using MSG. *IEEE Transactions on Geoscience and Remote Sensing*. **2006**, *44(10)*, 2761-2768.
17. Roberts, G.J.; Wooster, M.J. Fire detection and fire characterization over Africa using Meteosat SEVIRI. *IEEE Transactions on Geoscience and Remote Sensing*. **2008**, *46(4)*, 1200-1218.
18. Amraoui, M.; DaCamara, C.C.; Pereira, J.M.C. Detection and monitoring of African vegetation fires using MSG-SEVIRI imagery. *Remote sensing of Environment*. **2010**, *114(5)*, 1038-1052.
19. Laneve, G.; Jahjah, M.; Ferrucci, F.; Battazza, F. SIGRI project: the development of the fire vulnerability index. *In 34th International Symposium on Remote Sensing of Environment*; Sydney, **2011**, 10-15 April.
20. Laneve, G.; Cadau, E.; Ferrucci, F.; Rongo, R.; Guarino, A.; Fortunato, G.; Loizzo, R. SIGRI-an Integrated System for Detecting, Monitoring, Characterizing Forest Fires and Assessing damage by LEO-GEO Data. *Italian Journal of Remote Sensing*. **2012**, *44(1)*, 19-25.
21. Laneve, G.; Jahjah, M.; Ferrucci, F.; Hirn, B.; Battazza, F.; Fusilli, L.; De Bonis, R. SIGRI project: Products validation results. *IEEE Journal of Selected Topics in Applied Earth Observations and Remote Sensing*. **2014**, *7(3)*, 895-905.
22. Schmid, J. The SEVIRI instrument. Proceedings of the 2000 EUMETSAT Meteorological Satellite Data User's Conference, Bologna, Italy. Vol. 29. 2000.
23. Saunders, R.W.; Kriebel, K.T. An improved method for detecting clear sky and cloudy radiances from AVHRR data. *International Journal of Remote Sensing*. **1988**, *9(1)*, 123-150.
24. Dozier, J. A method for satellite identification of surface temperature fields of subpixel resolution. *Remote Sensing of environment*. **1981**, *11*, 221-229.
25. Zhukov, B.; Lorenz, E.; Oertel, D.; Wooster, M.; Roberts, G. Spaceborne detection and characterization of fires during the bi-spectral infrared detection (BIRD) experimental small satellite mission (2001–2004). *Remote Sensing of Environment*. **2006**, *100(1)*, 29-51.
26. Wooster, M.J.; Roberts, G.; Perry, G.L.W.; Kaufman, Y.J. Retrieval of biomass combustion rates and totals from fire radiative power observations: FRP derivation and calibration relationships between biomass consumption and fire radiative energy release. *Journal of Geophysical Research: Atmospheres*. **2005**, *110(D24)*.
27. Laneve, G.; Cadau, E.G.; Santilli, G. Estimation of the burned biomass based on the quasi-continuous MSG/SEVIRI earth observation system. *In Geoscience and Remote Sensing Symposium, 2009 IEEE International, IGARSS*. **2009**, *3*, III-597.

 doi:10.20944/preprints201801.0007.v1

551 28. Sobrino, J.A.; Romaguera, M. Land surface temperature retrieval from MSG1-SEVIRI data. *Remote Sensing*
552 *of Environment*. **2004**, *92(2)*, 247-254.
553 29. Joro, S.; Samain, O.; Yildirim, A.; Van De Berg, L.; Lutz, H. J. Towards an improved active fire monitoring
554 product for MSG satellites. *EUMETSAT*; 2008.